# Effect of ball-burnishing on hydrogen-assisted cracking of a martensitic stainless steel

Alixe Dreano, Michella Alnajjar, Ferdinando Salvatore, Joël Rech, Cédric Bosch, Krzysztof Wolski, Guillaume Kermouche, Frédéric Christien

# Effect of ball-burnishing on hydrogen-assisted cracking of a martensitic stainless steel

A. Dreano[1], M. Alnajjar[1], F. Salvatore[2], J. Rech[2], C. Bosch[1], K. Wolski[1], G. Kermouche[1], F. Christien[1]

[1] Mines Saint-Etienne, Univ Lyon, CNRS, UMR 5307 LGF, F - 42023 Saint-Etienne, France
[2] Ecole Centrale de Lyon - ENISE, Univ Lyon, CNRS, UMR5513 LTDS, 58 Rue Jean Parot, 42000 Saint-Etienne, France

**Abstract**

Slow strain rate tensile tests under hydrogen cathodic charging are conducted on 17-4 PH steel with two surface conditions: mirror polished and ball-burnished. In both cases, significant subcritical cracking initiating at the surface is observed leading to considerable reduction in elongation to fracture. However, ball-burnished specimens show better elongation and much less secondary cracking than the polished ones. Ball-burnishing introduces high compressive residual stresses in the specimen sub-surface. However, EBSD showed a very limited impact of ball-burnishing on the microstructure, so little effect on hydrogen trapping is expected. The beneficial effect of ball-burnishing on the resistance of the hydrogen assisted cracking is mainly explained by the high compressive longitudinal stress at the specimen surface, which makes crack initiation more difficult and hence delays specimen failure. In addition, it is estimated that the amount of hydrogen introduced at the specimen surface is decreased by approximately 30% due to the high compressive hydrostatic stress.

**Keywords**
Hydrogen embrittlement, ball-burnishing, maraging stainless steel, residual stress, sub-critical cracking

## 1. Introduction

Precipitation hardenable stainless steel are used for a variety of applications such as chemical plants, marine environment or oil and gas industry. More particularly, 17-4 PH contains 15 – 17.5 wt.% of chromium, allowing the formation of an adherent and protective passive layer at the surface, 3-5 wt.% of nickel and 3-5 wt.% of copper. The 17-4 PH exhibits a martensitic microstructure after solution heat treatment and quenching. An ageing treatment applied in the range of 480 – 620°C can also be applied, resulting in strengthening due to the precipitation of a Cu-rich phase in the martensitic matrix [1,2]. This alloy is one of the most popular among the precipitation hardenable stainless steels because of its high tensile strength, corrosion resistance and fracture toughness. However, several studies showed that it is very sensitive to hydrogen embrittlement [3–6].

In a previous work [3], the mechanical behavior of 17-4 PH was studied through slow strain rate tensile (SSRT) tests under cathodic charging. In air, the material exhibits a ductile fracture whereas a fragile intergranular fracture is observed with hydrogen. It appears that the brittleness is due to a subcritical crack growth, where hydrogen interacts with the crack tip. The cracks initiate at the specimen surface where the hydrogen concentration is usually the highest. Such a hydrogen-assisted phenomenon is usually observed during SSRT tests under hydrogen [7,8]. In such case, the diffusion distance of hydrogen during the experiment can be much smaller than the crack length, indicating that the hydrogen source moves along with the crack propagation [7,9] and interacts with the crack tip.

17-4 PH has a complex microstructure with the presence of a martensitic matrix, copper precipitates and austenite [3]. After solution heat treatment at 1050°C, the former austenitic grain size is about 15 to 20 µm [10]. The former austenitic grains are divided into martensite packets, blocks and laths [11].

The block and lath size is of the order of 3 µm [3] and 500 nm [12], respectively. Using atom probe tomography, Yeli *et al.* [13] showed that, after ageing for 2 hours at 590°C, the number density and mean radius of copper precipitates were 4.3 $10^{22}$ $m^{-3}$ and 5.5 nm, respectively. According to a recent study by Schutz *et al.* [14], copper precipitates have a face centered cubic (FCC) structure for ageing treatments above 550°C, with orientation relationship with the matrix. Austenite is also present, either as retained austenite or as reverted austenite, the latter forming during the ageing treatment. Alnajjar *et al.* [3] measured a fraction of austenite of 5.2% after ageing for 4 hours at 580°C. Austenite is present as thin layers, about 50 nm in thickness, along the lath boundaries [2]. Dislocation density in 17-4PH steel was studied in details by Christien *et al.* [15]. In the quenched state, the dislocation density is as high as a few $10^{15}$ $m^{-2}$, but this value drops to a few $10^{14}$ $m^{-2}$ after ageing at 600°C for four hours.

Such microstructure induces a high trapping effect of hydrogen. Using hydrogen permeation, Alnajjar *et al.* [3] measured an apparent hydrogen diffusion coefficient of 2.3 $10^{13}$ $m^2$ $s^{-1}$ in 17-4PH steel aged for 4 hours at 580°C. This is lower by four orders of magnitude than the hydrogen diffusion coefficient in bcc iron [16], showing the effect of the steel microstructure on hydrogen trapping. Using permeation and TDS on different heat treatments of 17-4PH steel, Schutz *et al.* [14] showed that the most active traps for hydrogen were copper precipitates and austenite. Concerning trapping by the copper precipitates, they suggested that hydrogen is mainly trapped at the precipitate-matrix interface.

Several works tried to identify some relations between hydrogen microstructural trapping steel and hydrogen embrittlement of 17-4PH steel. Some studies pointed out the effect of the prior austenite grain size on hydrogen embrittlement [4,17,18]. Increasing the austenitizing temperature results in coarser grain structure and then to a decrease of the grain boundaries length. By decreasing the proportion of grain boundaries, less hydrogen is trapped and hydrogen embrittlement susceptibility could be modified accordingly. However, the difficulty of such studies is to decouple the effect of prior austenite grain size to other microstructural modifications due to heat treatments. Indeed, some studies showed an effect of heat treatments on hydrogen trapping and embrittlement [4–6]. For example, Chiang and co-authors [5] showed that the solution annealed specimen exhibit a better resistance to hydrogen embrittlement than the peak-aged specimen. They concluded that the hydrogen trapped in the Cu-rich precipitate –matrix interface cause the brittle fracture of peak-aged 17-4 PH, although direct comparison between the solution annealed and peak-aged state is difficult as these two states have very different initial mechanical properties. Shen and co-authors [4] on the contrary demonstrated a beneficial effect of copper precipitation on hydrogen embrittlement susceptibility when the solution-treatment temperature increases. Hayashi *et al.* [6] confirmed the beneficial effect of precipitates on hydrogen embrittlement by a trapping effect. However, such effect disappeared when hydrogen was trapped in both precipitates and matrix. Again, these studies showed the high trapping effect of precipitates. However, the role of such traps on hydrogen embrittlement is still unclear.

Many researches were conducted to prevent hydrogen embrittlement. For example, the use of "hydrogen-resistant coatings" were considered to act as a diffusion barrier on the material surface [19,20]. Several coatings were tested such as stable oxides formed at the surface, cadmium or nickel plating or hard coatings. The limitation of such technologies is mainly due to coating defects and the necessity to be completely adherent to pursue its hydrogen-resistant properties [19,20]. Mechanical treatments of the surface were then considered to prevent hydrogen embrittlement. Several authors showed a beneficial effect of pre-straining [21,22] or peening technologies [23–25] to mitigate hydrogen embrittlement. Such mechanically transformed surface was investigated to determine the role of residual stress and plastic deformation on hydrogen diffusion and embrittlement. It mainly appears that plastic deformation plays an important role to inhibit the diffusion of hydrogen towards the bulk material by favoring trapping. Indeed, the decrease in grain size or the increase in dislocation density at the surface lead to an increase in the apparent solubility and a decrease in the apparent diffusivity [23,25,26]. The introduction of compressive residual stress (CRS) at the surface also plays a

role to mitigate hydrogen embrittlement. Takakuwa and co-authors [27,28] showed that the hydrostatic stress field around the crack tip can be greatly reduced by compressive residual stress, which then reduces the hydrogen concentration in the critical zone. Hence, the introduction of CRS delays the initiation and the growth of cracks, not only in hydrogen-rich environment.

In the present paper, it is proposed to study the effect of a superfinishing process, ball-burnishing, on 17-4 PH hydrogen-assisted cracking. Burnishing is a simple and low-cost process which improves the surface integrity (roughness, residual stress, microstructure, hardness) of materials [29,30]. For example, ball-burnishing has a beneficial effect on fatigue lifetime [31], wear [32] or corrosion resistance [33]. 17-4 PH is a low work hardening rate material with high yield stress so it is expected that ball-burnishing, with the absence of sliding, only implements compressive residual stress during the surface treatment [34].

## 2. Experimental procedures

### 2.1. Studied material

The material used in this study is a wrought 17-4 PH steel whose composition is provided in Table 1. The axisymmetric slow strain rate tensile test samples are cut into the commercial bar and have a gage length of 10 mm with a diameter of 5 mm. Samples have undergone a solution heat treatment at 1050°C for 1 h followed by a water quenching and an ageing treatment at 580°C for 4 h. The tensile specimens were also polished up to 1 µm diamond finish using a lathe.

Table 1 : Chemical composition of the 17-4 PH steel used in this work in wt. % provided by supplier.

| C | Ni | Si | P | Mn | Cr | Cu | S | Nb | Fe |
|---|---|---|---|---|---|---|---|---|---|
| 0.031 | 4.82 | 0.31 | 0.016 | 0.81 | 15.61 | 3.12 | 0.02 | 0.21 | Bal. |

### 2.2. Ball-burnishing procedure

The ball-burnishing process is a mechanical surface treatment (Figure 1) where a normal pressure is applied to the machined surface using a rigid rolling ball. The process induces a cold plastic deformation of the roughness peaks of the surface. From a macroscopic point of view, no sliding occurs between the ball and the machined surface. Ball-burnishing has been performed within the following conditions: ball diameter $\Phi$ = 6mm; rolling velocity (or burnishing speed) $v_g$ = 50 m/min; feed per revolution $f$ = 0.2 mm and normal force $F_n$ = 250N. Some specimens were ball-burnished before the tensile experiments and are denoted “ball-burnished specimens” in the following. The specimens that did not undergo ball-burnishing are denoted “polished sample” since a polishing procedure was applied (see sub-section 2.1).

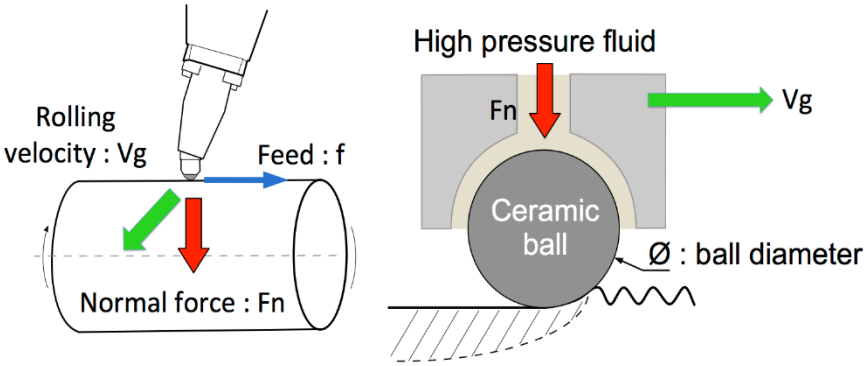


Figure 1 : Principle of the ball-burnishing process (reprinted from [29] with permission from Elsevier).

### 2.3. X-ray diffraction measurements

Residual stresses were measured on polished and ball-burnished cylindrical tensile specimens. Measurements were conducted in both the longitudinal and transverse directions using an X-ray diffractometer of type STRESSTECH Xstress 3000. The conditions of measurement are given in Table 2.

Table 2 : Experimental conditions of residual stress measurements.

| Diffraction Conditions | Acquisition conditions |
|---|---|
| • Cr Kα source ($\lambda$ = 0.2291 nm) operated at 28 kV and 6 mA<br>• (211) plane, $2\theta$ = 156.4° | • $\psi$ mode<br>• 17 $\psi$ angles from -45° to +45°<br>• $\psi$ oscillation : ± 6° |

The in-depth residual stresses were measured after layer-by-layer material removal using local electro-dissolution under 13V in an ammonium chloride solution. After each layer removal, the depth was measured using an INTRA Talysurf profilometer from Taylor Hobson. Peak breadths (FWHM: full width at half maximum) were also extracted from the X-ray diffraction measurements. The diffraction peak breadth in the kind of materials studied here is mainly related to the dislocation density [15,35].

### 2.4. Roughness measurements

Surface roughness was measured on polished and ball-burnished cylindrical tensile specimens thanks to a focus variation microscope mounted with a 50x objective. The vertical resolution was of 30 nm and the lateral resolution was of 2 µm for a scanning area of 1x1 mm². A cut off filter of 800 µm was used and the surface waviness was removed using the appropriate filter.

### 2.5. Slow Strain Rate Tensile tests

Ball-burnished and polished specimens were tested at room temperature at a displacement rate of $10^{-5}$ mm/s and $10^{-4}$ mm/s with or without electrochemical hydrogen charging. The tensile machine used for the experiments is a SCHENK machine where a LVDT is mounted in order to record the displacement. A correction is applied on raw data as the LVDT is fixed outside the electrochemical cell, i.e. not on the specimen itself.

For each surface condition (ball-burnished or polished surface), tensile tests were performed in air and under cathodic charging. Some specimens were pre-charged for 24 h before the SSRT test began and remained under charging until the fracture happened. Such tests are denoted “H pre-charged”. Other specimens were only charged during the tensile tests and are denoted “H charged”. All samples were cathodically charged at – 800 mV using a PGP201 potentiostat. A saturated calomel electrode is used as a reference electrode and a platinum grid as a counter electrode. The charging procedure was done using a 30 g/l NaCl + 0.4 g/l sodium acetate solution with a pH of 1.5. The solution was deaerated with nitrogen gas before and during the test. The electrochemical cell and the sample are mounted on the tensile machine and purged with nitrogen before the solution is introduced. The cathodic charging was launched when the three electrodes were immersed. After the SSRT test, the specimens were unmounted and cleaned with ethanol for fractographic observation.

### 2.6. Microstructural observations using EBSD

For EBSD observations, the samples were cut following the transverse direction. The section was polished up to 1200 grit followed by electropolishing using 94% ethanol + 6% perchloric acid as an electrolyte at 25 V during 60 s. A Zeiss SEM was used at 20 kV for EBSD.

### 2.7. Hardness measurements

The same specimen as for EBSD observations were used for nanoindentation measurements in the sub-surface. Berkovich nanoindentation grids (100x600 µm) were carried out to evidence modifications of mechanical properties induced by the burnishing operation using a DCM

nanoindentation set up (MTS). The penetration depth was set to 300 nm and space between indents was about 20 µm. Hardness and elastic modulus were extracted using Loubet's method [36].

## 3. Results and discussion

### 3.1. Surface modifications due to ball-burnishing

#### *3.1.1.Roughness measurements*

Table 3 presents the roughness of polished and ball-burnished specimens. As expected, the roughness of the ball-burnished material is low, around 0.4 µm. For the polished material, the roughness is around 0.5 µm. Escobar and co-authors [37] have shown that the surface roughness of a high-strength low-alloy steel can affect the quantity of hydrogen absorbed by the surface during electrochemical charging. However, a significant effect is observed when the roughness varies by a factor of 100. Hence, it can be safely concluded that, in this study, the roughness will not affect the electrochemical charging and then the quantity of absorbed hydrogen. Then, it is considered here that the roughness is very low and similar for the two materials.

Table 3 : Roughness measurements for the polished and ball-burnished samples.

| | Polished material | Ball-burnished material |
|---|---|---|
| Ra (µm) | 0.49 | 0.37 |

#### *3.1.2.Microstructural observations*

Figure 2 shows the EBSD results obtained on a cross-section of a ball-burnished specimen. The bottom of the maps corresponds to the ball-burnished surface and the mapped area covers 200 µm below it. Figure 2a is the orientation map (IPF z, z being the normal to the observed surface). Grain boundaries of misorientation higher than 10° are highlighted in black. Those "grains" actually correspond to martensite blocks, as described in details in [11]. No significant deformation of the morphological texture, i.e. shape of the martensite blocks, is observed close to the ball-burnished surface.

Figure 2b shows the first order KAM map obtained from the EBSD data. The first order KAM (Kernel Average Misorientation) is the misorientation between a given pixel of the map and the first order neighboring pixels. Local misorientations are observed inside the martensite blocks. In addition, the highest local misorientations, corresponding to the yellow areas in Figure 2b, are concentrated in "walls". This is consistent with the existence, in a given martensite block, of several slightly misoriented martensite laths, that can be described as dislocations walls [11]. Additionally, an increase in local misorientation is observed at the bottom of Figure 2b, i.e. in the vicinity of the ball-burnished surface. This suggests that ball-burnishing has plastically deformed the sub-surface of the specimen.

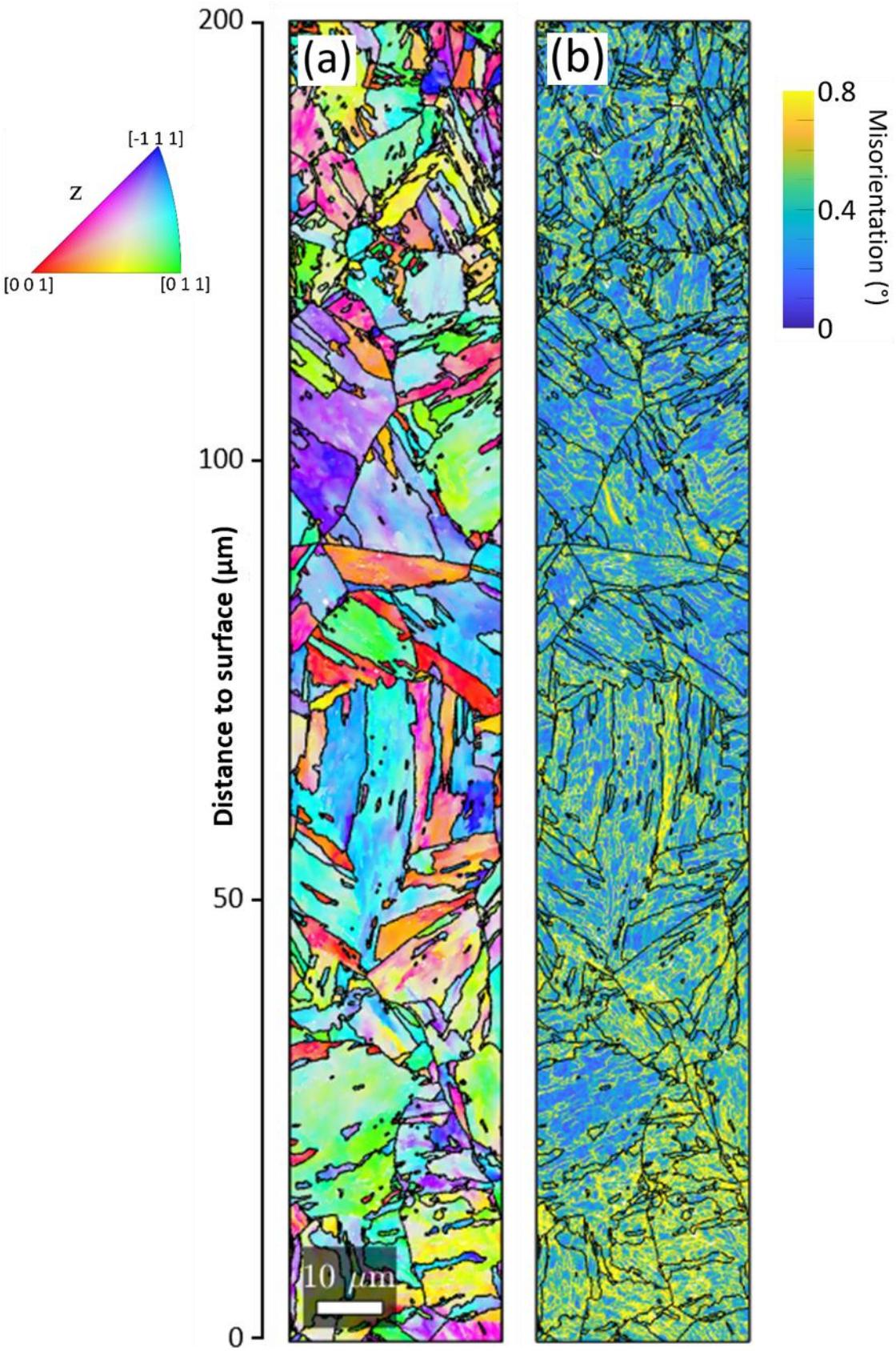


Figure 2 : EBSD analysis on a cross-section of the ball-burnished material : (a) orientation map (IPFz) ; (b) kernel average misorientation map. The bottom of the figure corresponds to the ball-burnished surface.

Figure 3 shows the variation of the local misorientation with the distance to surface. This was obtained by averaging the data of Figure 2b line by line. The KAM is observed to increase from 0.5° to 0.8° over

the depth investigated here (200 µm). Assuming that the density of geometrically necessary dislocations (GNDs) is proportional to the KAM [38], this would imply an increase of the GND density by a factor of the order of 1.5 in the close sub-surface, due to ball-burnishing. However, this increase in KAM observed in Figure 3 has to be considered with caution as it is not much higher than the level of noise [38].

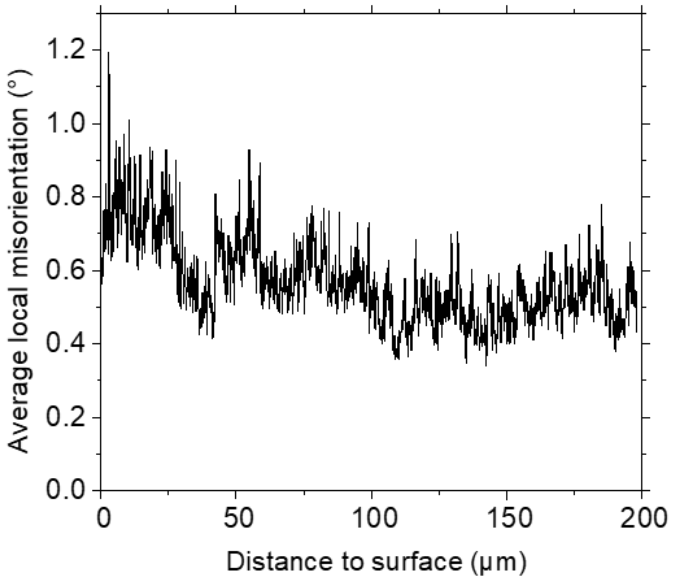


Figure 3 : Average kernel misorientation as a function of the distance to the ball-burnished surface, extracted from Figure 2b.

Figure 4 shows the depth-dependence of the X-ray diffraction peak breadth (FWHM). Similar values of FWHM are found in the transverse and longitudinal directions. Data in Figure 4 are the transverse-longitudinal average values. An increase in the diffraction peak breadth from 2.5° to 3° is observed within the 200 µm beneath the surface. Following the approach proposed in [15] and [35], the additional dislocation density corresponding to such a peak broadening can be roughly estimated at ~$10^{14}$ $m^{-2}$, which is of the same order as the initial dislocation density present in the material bulk.

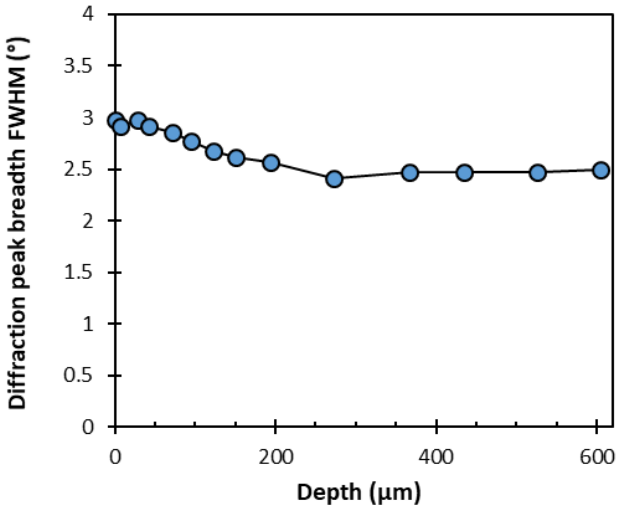


Figure 4 : Diffraction peak breadth (FWHM) as a function of the distance to the ball burnished surface

*3.1.3. Hardness and residual stresses profiles*

Figure 5a present the evolution of the hardness and the elastic modulus from the surface towards the bulk for the ball-burnished specimen. An increase in hardness is observed at the vicinity of the surface and tends to slowly decrease to stabilize around 500 µm below the surface. It should be noted that the increase is only of about 7% ($H$ = 4.2 GPa at the surface and $H$ = 3.9 GPa in the bulk). The elastic modulus also varies from surface to depth with an increase of less than 5% ($E$ = 190 GPa at the surface and $E$ = 180 GPa in the bulk).

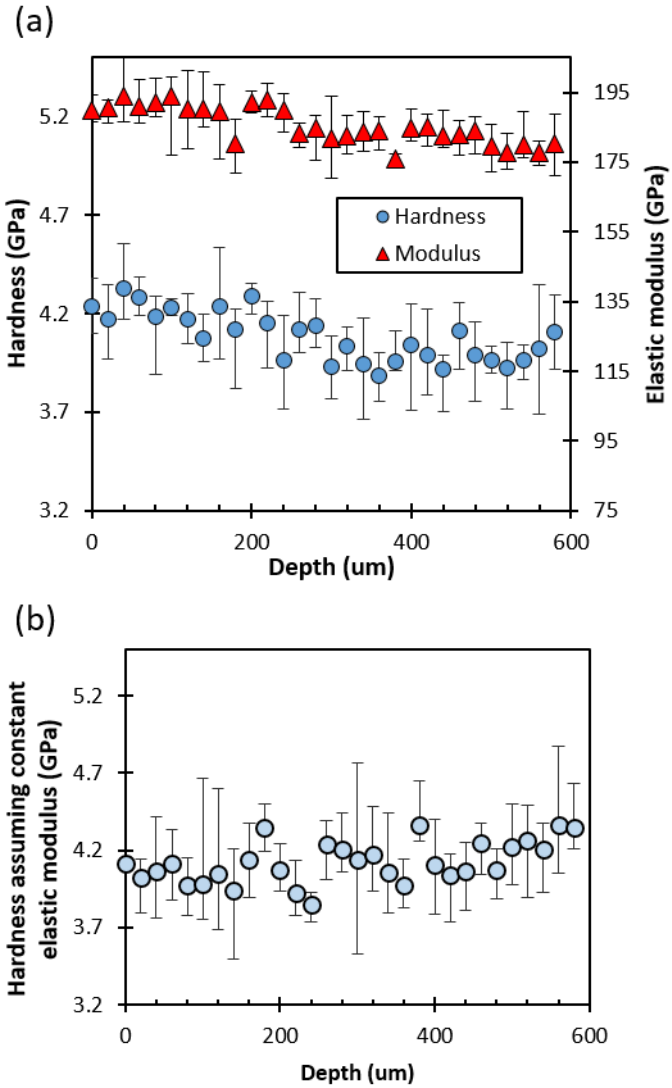


Figure 5 : (a) Hardness and elastic modulus in-depth profiles of the ball-burnished specimen ; (b) Hardness in-depth profile of the ball-burnished specimen computed from nanoindentation measurements considering a constant Young modulus (185 GPa)

Figure 6 presents the evolution of the residual stress before and after the ball-burnishing process. High compressive residual stress (CRS) are observed for the ball-burnished specimen over the first hundreds of micrometers, around -600 and -800 MPa. For the polished specimen, it appears that the CRS is very limited, reaching only -110 MPa over the first ten micrometers.

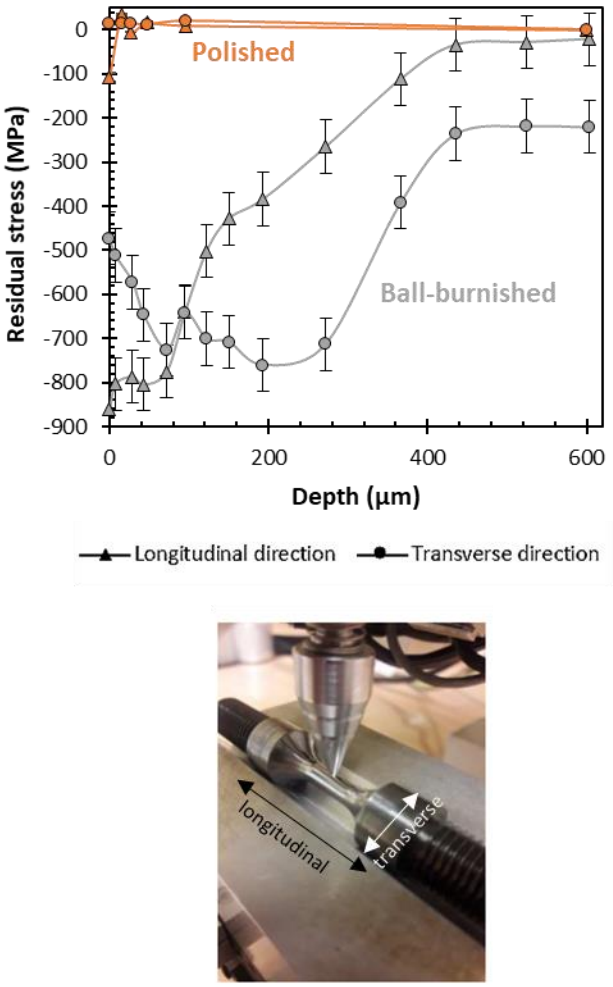


Figure 6 : Residual stress depth profiles for the ball-burnished and polished specimens.

It was previously showed that residual stresses can have a significant effect on the hardness and elastic modulus obtained from nanoindentation measurements [39,40]. Indeed, residual compressive stresses are known to lead to an apparent hardness increase related to the decrease of the penetration depth for a given indentation load. The same conclusion holds for the elastic modulus. In absence of residual stresses, the elastic modulus should not depend upon any mechanical surface treatment inducing plastic flow. The noticed variation is a clear signature of residual stresses. For instance, computing the hardness profile assuming a constant elastic modulus of 185 GPa leads to a roughly constant hardness versus depth (Figure 5b). Such method was previously used by Breumier *et al.* [41] to reveal shot-peening induced strain hardening.

The effects of residual stress on nanoindentation hardness is usually a second-order effect compared to plastic flow induced strain-hardening, except for low work-hardening rate materials such as 17-4 PH. In this latter case, the yield stress reaches saturation after a few percent of plastic deformation, when Berkovich or Vickers indentation tests are known to probe metals yield stress for a ~8% plastic strain level [42]. Note that, as the specimen was cut for hardness measurement, the longitudinal stress was suppressed and only the transverse stress applies here.

In summary, no significant increase in hardness was observed due to ball-burnishing. This shows that the increase in dislocation density shown in Figure 3 and in Figure 4 does not significantly affect the material hardness. This is consistent with the analysis of the strengthening mechanisms by Alnajjar et al [3], showing only a limited contribution of work-hardening to the hardness of aged 17-4PH steel.

3.2. Mechanical results

*3.2.1.Slow strain rate tensile test*

Figure 7a presents the engineering stress-strain curves obtained for the ball-burnished (full line) and polished (dotted line) specimens when tested in air (at $10^{-5}$ mm/s) and in hydrogen-rich environment (H charged at $10^{-4}$ mm/s , H pre-charged at $10^{-4}$ mm/s and H pre-charged at $10^{-5}$ mm/s). The engineering stress was calculated by dividing the load with the minimal cross-section obtained along the tensile axis.

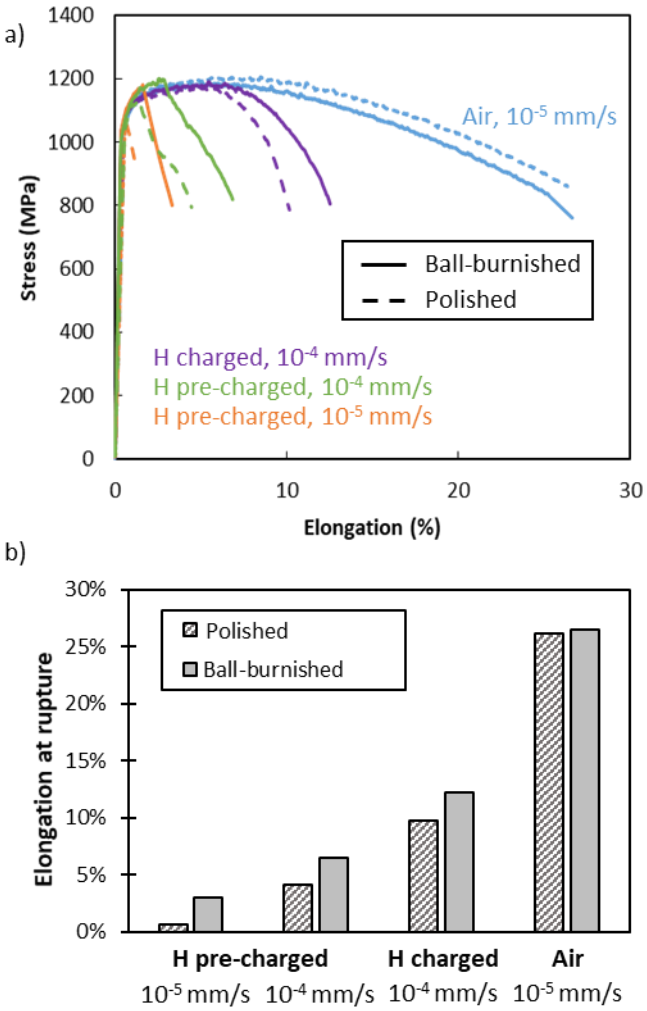


Figure 7 : (a) Slow strain rate tensile test curves ; (b) Elongation at fracture for the two materials in the different H charging conditions tested

A significant elongation (about 26%) is observed for the polished specimens in air (Figure 7b). When tested in hydrogen environment, a pronounced effect of hydrogen is observed for the polished specimens compared to air. Indeed, as presented in Figure 7b, the elongation decreases to 9.7% for the H charged, $10^{-4}$ mm/s condition, to 4.1% for the H pre-charged, $10^{-4}$ mm/s condition and to only 0.7% for the H pre-charged, $10^{-5}$ mm/s condition. A strong effect of the hydrogen charging condition is observed. After ball-burnishing, the specimens present a systematic increase in the elongation at rupture when tested in hydrogen environment (Figure 7b) compared to air. Hence, a small but systematic beneficial influence of the ball-burnishing process is observed on the hydrogen embrittlement susceptibility.

*3.2.2.Fractographs and fracture mode*

In a previous work [3], it was showed that 17-4 PH presents a ductile fracture when tested in air, indicated by the presence of a reduction of area, dimples and shearing lips. The same conclusion is made when the fracture of the ball-burnished specimens tested in air is observed (not show here). Figure 8 presents the fracture surface of the polished and ball-burnished specimens tested for H charged at $10^{-4}$ mm/s. Such images are representative of what is observed for all the hydrogen charged tested conditions. Both polished and ball-burnished surfaces present no reduction in area after the SSRT experiments. The fractures surface are composed of a brittle area near the edges and a ductile zone at the centre (Figure 8a & d). The brittle zone is entirely intergranular (Figure 8b & e) whereas the ductile zone is revealed by the presence of dimples (Figure 8c & f).

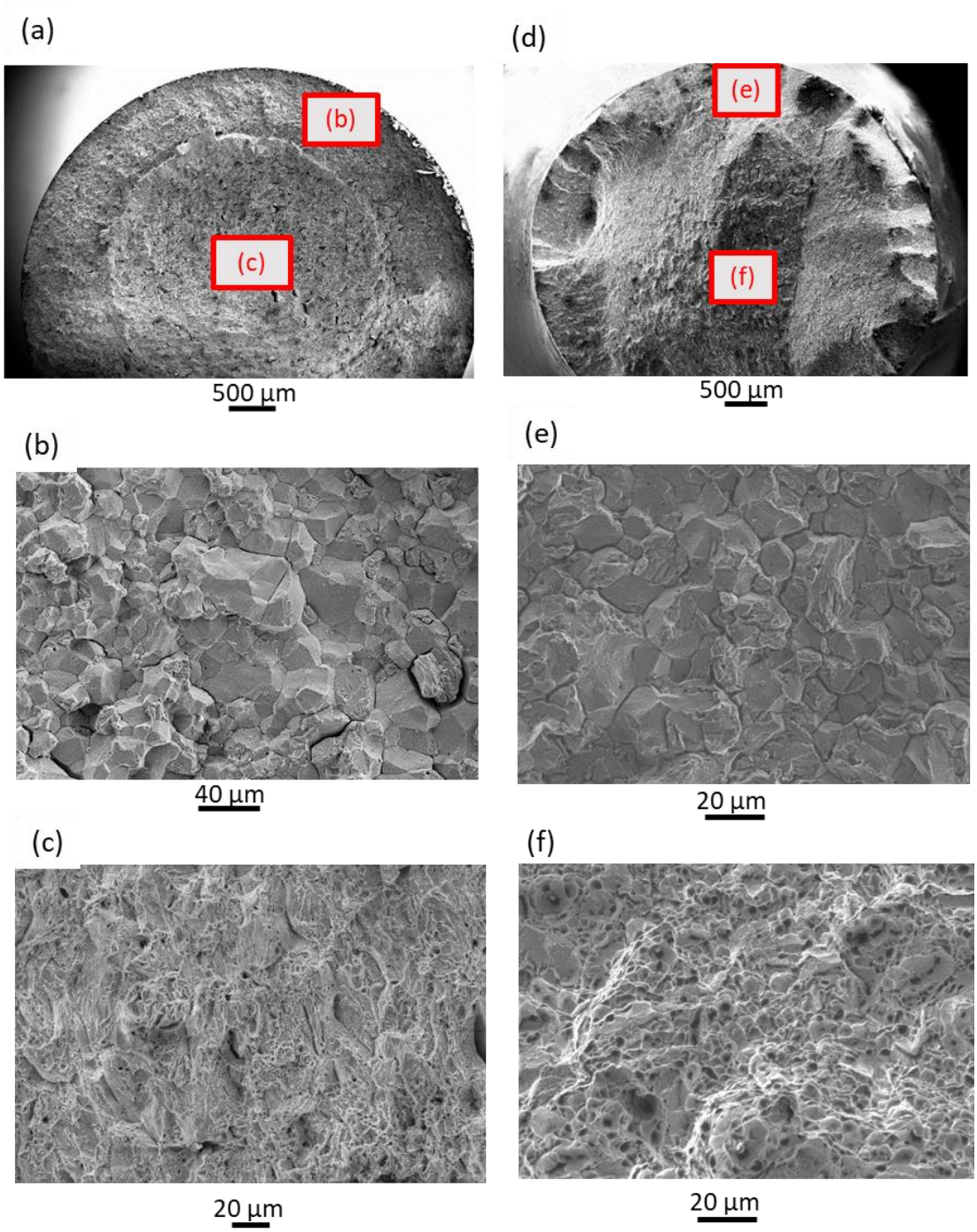


Figure 8 : Fracture surfaces after tensile test for the polished specimens (a-c) and the ball-burnished specimens (d-f) for the H charged, $10^{-4}$ mm/s condition.

Figure 9 shows a side view of the polished and ball-burnished specimens after the tensile test in H charged, $10^{-4}$ mm/s condition. The same observations are made in the other H charging conditions. Secondary cracks are observed over the surface of the polished and ball-burnished specimens. Those cracks, which did not induce the final fracture, demonstrate the occurrence of subcritical crack growth occurring for all the tested conditions. The fracture can be described into three steps [3]:

- Formation of multiple subcritical cracks,
- Coalescence of some of them to form the main crack that propagates up to a critical length,
- Final overload of the remaining ligament inducing the fracture.

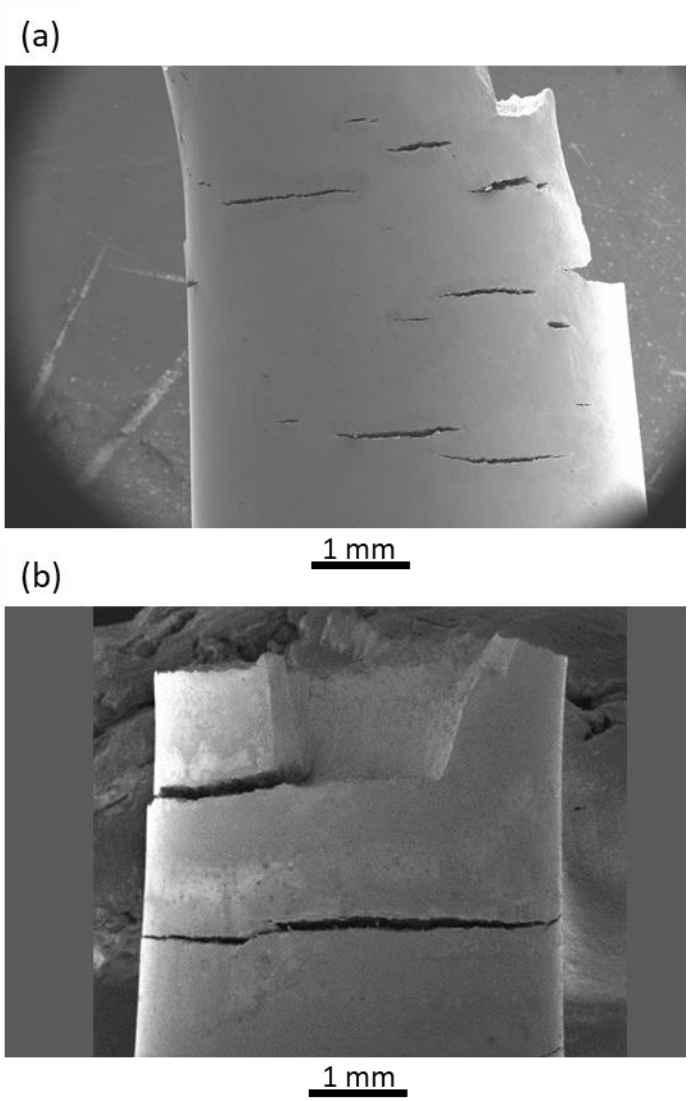


Figure 9 : Side views showing secondary cracking for: (a) the polished specimen ; (b) the ball-burnished specimen at $10^{-4}$ mm/s, pre-charged conditions.

Figure 7a confirms the subcritical crack growth. Indeed, a decrease in load in observed for the samples tested in hydrogen environment, while no necking is observed on the fracture micrographs presented in Figure 8. Such load drop is attributed to the propagation and coalescence of cracks, inducing a decrease of the specimen's rigidity and then a load drop. Finally, as previously observed [3], the load drops are very slow for all the tested condition (ball-burnished and polished specimens), ranging from 2 hours to 59 hours depending on the testing conditions (

Table 4). For polished and ball-burnished specimens, hydrogen has sufficient time to interact with the crack tips. From these results, it is concluded that there is no significant difference in the degradation mechanism under hydrogen environment between the polished and the ball-burnished specimens. However, degradation is delayed for the ball-burnished specimens.

Table 4 : Duration of load drop on the SSRT curves depending on the different charging conditions and specimens.

| | Duration of load drop (h) | |
|---|---|---|
| | Polished specimens | Ball-burnished specimens |
| H charged – $10^{-4}$ mm/s | 3.7 | 5.3 |
| H pre-charged – $10^{-4}$ mm/s | 2.75 | 3.7 |
| H pre-charged – $10^{-5}$ mm/s | 22 | 59 |

### 3.3. Discussion

Results have shown that ball-burnishing induces a systematic decrease in the hydrogen embrittlement susceptibility (Figure 7) by introducing a delaying effect on the degradation mechanism.

First, the question of a possible effect of ball-burnishing on the dislocation density and associated hydrogen trapping in the sub-surface deserves consideration. The analysis of local crystal misorientation (Figure 3) and diffraction peak broadening (Figure 4) have shown that ball-burnishing increases the initial dislocation density by a factor of 1.5 to 2 at the specimen surface. However, to know if this can significantly affect hydrogen trapping, the trapping capacity of the different types of traps has to be estimated. Assuming that the number of trapping sites per dislocation length is 10 $nm^{-1}$ [43], a dislocation density of 5 $10^{14}$ $m^{-2}$ (corresponding approximately to the dislocation density at the surface of the bull burnished specimens) gives a trapping site volume density of 5 $10^{24}$ $m^{-3}$. On the other hand, considering the martensitic block size of 3 µm, the block boundary density is $10^{6}$ $m^{-1}$. Assuming one trapping site per Bürgers vector squared [44], a trapping site density of 1.6 $10^{25}$ $m^{-3}$ is obtained in block boundaries. The same estimation for the copper precipitate – matrix interfaces can be made. Considering the volume density and size of precipitates measured by Yeli et al. [13] after ageing at 590°C, the precipitate-matrix interface density obtained is as high as 1.6 $10^{7}$ $m^{-1}$, corresponding to a trapping site density of 2.6 $10^{26}$ $m^{-3}$. For austenite – martensite interfaces, assuming an austenite fraction of 5% [3] and a thickness of austenite layers of 50 nm [2], an austenite – martensite interface density of 2 $10^{6}$ $m^{-1}$ is obtained, corresponding to a trapping site density of 3.3 $10^{25}$ $m^{-3}$. Numerical data are summarized in Table 5.

Table 5 : Estimation of the trapping site density for 17 4 PH steel for the ball-burnished specimen

| Type of traps | Estimation of the trapping site density |
|---|---|
| Dislocations | 5 $10^{24}$ $m^{-3}$ |
| Martensitic block boundaries | 1.6 $10^{25}$ $m^{-3}$ |
| Copper precipitate – matrix interfaces | 2.6 $10^{26}$ $m^{-3}$ |
| Austenite – martensite interfaces | 3.3 $10^{25}$ $m^{-3}$ |

By adding the contributions of the different types of interfaces, a total trapping site density of 2 $10^{26}$ $m^{-3}$ on interfaces is obtained. This estimation shows that the trapping capacity of interfaces, especially copper precipitate – matrix interfaces, is higher by almost two orders of magnitude than that of dislocations. This is in agreement with the conclusions by Schutz *et al.* [14], showing that the precipitate – matrix interfaces are the main trapping sites in 17-4PH steel. Hence, it can be safely concluded that the increase in dislocation density due to ball-burnishing in this material is not going to affect significantly the hydrogen trapping capacity, that is mainly governed by interfaces.

One the other hand, one has to consider the hydrostatic pressure effect on the diffusion kinetics of hydrogen. The effect of stress on equilibrium hydrogen concentration is given by Equation (2) that can be obtained by equalizing the chemical potential for a stressed and unstressed material in a given hydrogen-rich environment [45,46]:

$$c_\sigma = c_0 \exp\left(\frac{\sigma_h V_H}{RT}\right) \quad (2)$$

Where $c_\sigma$ is the hydrogen concentration in the stressed region, $c_0$ is the concentration in absence of stress, $\sigma_h$ is the hydrostatic stress : $\sigma_h = \frac{1}{3}(\sigma_{11} + \sigma_{22} + \sigma_{33})$ and $V_H$ is the partial molar volume of hydrogen (equals to 2 $cm^3$/mol for steels [25,47]). For the ball-burnished specimens, a biaxial compressive stress exists close to the specimen surface. Considering the stress profiles shown in Figure 6, the depth dependence of the hydrostatic stress can be obtained and introduced into Equation (2). Figure 10 presents the depth dependence of $c_\sigma/c_0$ thus obtained. It is to be mentioned that Equation (2) only applies at equilibrium, i.e. when the entire specimen thickness is equilibrated with the charging medium. This was not the case in the SSRT test conducted in this study because of the low hydrogen diffusion coefficient. However, it is obvious from Figure 10 that, due to the high CRS, the amount of hydrogen present in the subsurface may be lower by 30% in the ball-burnished specimens, compared to the polished specimens.

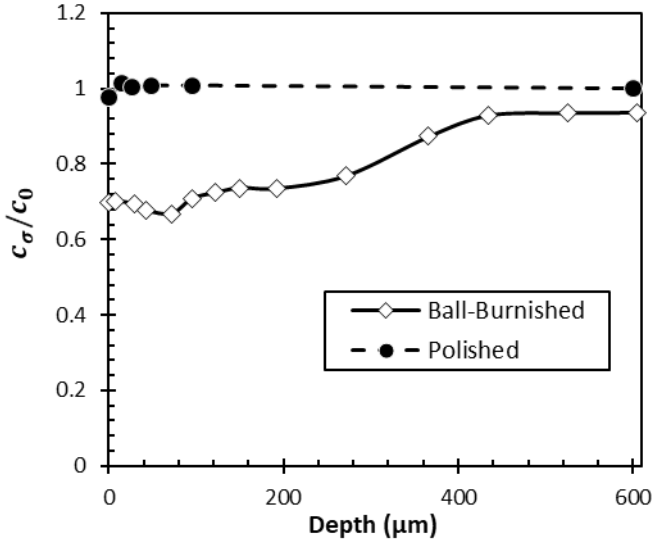


Figure 10 : Evolution of the $c_\sigma/c_0$ ratio for the ball-burnished and polished specimens obtained from Equation (2).

In addition, during tensile testing of the ball-burnished specimens, the subsurface remains under compression until the external tensile stress overcomes the longitudinal CRS, while the specimen bulk undergoes tension at any time. As crack initiation and propagation is possible only under a certain tensile stress, crack might initiate preferentially below the ball-burnishing affected layer (i.e. at a depth of ~500 µm), where the tensile stress and possibly the hydrogen concentration are higher (Figure 10). This scenario is of course possible only if hydrogen is able to travel a few hundreds of micrometers in a sufficiently short time. Considering the diffusion coefficient mentioned earlier (2.3 $10^{-13}$ $m^2$ $s^{-1}$), a hydrogen diffusion distance of 500 µm would require a diffusion time of twelve days ($t = \frac{x^2}{D}$, where $t$ is the time, $D$ the diffusion coefficient and $x$ the travelling distance), which is longer than any SSRT test conducted here. So, it seems that this mechanism, involving cracking below the ball-burnished affected layer, is rather unlikely. Moreover, all the cracks observed are connected to the specimen surface, so it is not possible to provide experimental evidence of such a mechanism.

Consequently, it is assumed that the cracks rather initiate at the specimen surface in both polished and ball-burnished specimens. In this scenario, it is obvious that the longitudinal CRS due to ball-burnishing is going to delay the initiation of cracks, that will not be possible until the external tensile stress has overcome the longitudinal CRS by a certain factor. In contrast, in the polished specimens, the tensile stress needed to initiate cracks will be reached earlier. In addition to this, the lower surface

hydrogen concentration in the ball-burnished specimens, compared to polished specimens (Figure 10) might also contribute to the retardation of surface crack initiation. This scenario could explain the beneficial effect of ball-burnishing on the resistance to hydrogen embrittlement on this material.

One final comment is due here about the secondary cracking observed on the side views of broken tensile specimens (Figure 9). Under the same testing conditions, the number of secondary cracks is significantly higher in the polished specimen than in the ball-burnished ones. This observation shows that crack initiation is less probable in the ball-burnished specimen, which further demonstrates the beneficial effect of ball-burnishing. This can be simply interpreted by the maximum tensile stress reached at the specimen surface during the SSRT test. For the polished specimens, the maximum tensile stress reached at the surface is approximately the tensile strength of the material, i.e. about 1200 MPa. For the ball-burnished specimens however, the maximum net tensile strength reached during the SSRT test is only of about 400 MPa, corresponding to the difference between the maximum external tensile stress (about 1200 MPa) and the surface longitudinal CRS (800 MPa). This makes crack initiation less probable for ball-burnished specimens and results in less secondary cracks formed.

## 4. Conclusion

In this work, slow strain rate tests under hydrogen cathodic charging were conducted on polished and ball-burnished cylindrical specimens of 17-4 PH stainless maraging steel aged four hours at 580°C. The main results of this study can be summarised as follows:

- Ball-burnishing results in high compressive residual stress (up to 800 MPa) in the longitudinal and transverse directions over a depth of several hundreds of µm. However, it has limited impact on the sub-surface microstructure of the material;
- Under cathodic charging, hydrogen embrittlement of 17-4 PH steel is considerable; it is manifested by sub-critical intergranular cracking, which results in limited tensile elongation;
- Ball-burnished specimens show better resistance to hydrogen embrittlement than polished specimens. This is due to the high compressive longitudinal stress at the surface of ball-burnished specimens, which makes crack initiation more difficult and hence delays the specimen failure.
- Another possible beneficial contribution of ball-burnishing is that the amount of hydrogen introduced at the specimen surface is decreased by approximately 30% due to the high compressive hydrostatic stress.

**Acknowledgements**
Claire Roume, Gilles Blanc and Marilyne Mondon are acknowledged for their help in SSRT tests, specimen surface preparation and EBSD observation. The authors would like to acknowledge financial support from Institut CARNOT M.I.N.E.S (project #60678) and from LABEX MANUTECH-SISE (ANR-10-LABX-0075) of Université de Lyon, within the program “Investissements d’Avenir” (ANR-11-IDEX-0007) operated by the French National Research Agency (ANR).

**References**

[1] Hsiao CN, Chiou CS, Yang JR. Aging reactions in a 17-4 PH stainless steel. Mater Chem Phys 2002;74:134–42. https://doi.org/10.1016/S0254-0584(01)00460-6.
[2] Viswanathan UK, Banerjee S, Krishnan R. Effects of aging on the microstructure of 17-4 PH stainless steel. Mater Sci Eng 1988;104:181–9. https://doi.org/10.1016/0025-5416(88)90420-X.
[3] Alnajjar M, Christien F, Bosch C, Wolski K. A comparative study of microstructure and hydrogen embrittlement of selective laser melted and wrought 17–4 PH stainless steel. Mater Sci Eng A 2020;785:139363. https://doi.org/10.1016/j.msea.2020.139363.
[4] Shen S, Li X, Zhang P, Nan Y, Yang G, Song X. Effect of solution-treated temperature on hydrogen

embrittlement of 17-4 PH stainless steel. Mater Sci Eng A 2017;703:413–21. https://doi.org/10.1016/j.msea.2017.06.078.
[5] Chiang WC, Pu CC, Yu BL, Wu JK. Hydrogen susceptibility of 17-4 PH stainless steel. Mater Lett 2003;57:2485–8. https://doi.org/10.1016/S0167-577X(02)01298-3.
[6] Hayashi Y, Ito T, Nishimura Y, Takai K. The states of hydrogen and hydrogen embrittlement susceptibility of precipitation hardened SUS630 stainless steel. IOP Conf Ser Mater Sci Eng 2018;461:012023. https://doi.org/10.1088/1757-899X/461/1/012023.
[7] Martínez-Pañeda E, Harris ZD, Fuentes-Alonso S, Scully JR, Burns JT. On the suitability of slow strain rate tensile testing for assessing hydrogen embrittlement susceptibility. Corros Sci 2020;163:108291. https://doi.org/10.1016/j.corsci.2019.108291.
[8] Johnson HH, Troiano AR. Crack initiation in hydrogenated steel. Nature 1957;179:777. https://doi.org/10.1038/179777a0.
[9] Gangloff RP, Ha HM, Burns JT, Scully JR. Measurement and modeling of hydrogen environment-assisted cracking in monel K-500. Metall Mater Trans A Phys Metall Mater Sci 2014;45:3814–34. https://doi.org/10.1007/s11661-014-2324-z.
[10] Alnajjar M, Christien F, Wolski K, Bosch C. Evidence of austenite by-passing in a stainless steel obtained from laser melting additive manufacturing. Addit Manuf 2019;25:187–95. https://doi.org/10.1016/j.addma.2018.11.004.
[11] Morito S, Huang X, Furuhara T, Maki T, Hansen N. The morphology and crystallography of lath martensite in alloy steels. Acta Mater 2006;54:5323–31. https://doi.org/10.1016/j.actamat.2006.07.009.
[12] Guennouni N, Barroux A, Grosjean C, Maisonnette D, Nivet E, Andrieu E, et al. Comparative study of the microstructure between a laser beam melted 17-4PH stainless steel and its conventional counterpart. Mater Sci Eng A 2021;823:141718. https://doi.org/10.1016/j.msea.2021.141718.
[13] Yeli G, Auger MA, Wilford K, Smith GDW, Bagot PAJ, Moody MP. Sequential nucleation of phases in a 17-4PH steel: Microstructural characterisation and mechanical properties. Acta Mater 2017;125:38–49. https://doi.org/10.1016/j.actamat.2016.11.052.
[14] Schutz P, Martin F, Auzoux Q, Adem J, Rauch EF, Wouters Y, et al. Hydrogen transport in 17-4 PH stainless steel : influence of the metallurgic state on hydrogen diffusion and trapping Keywords : n.d.:1–20.
[15] Christien F, Telling MTF, Knight KS. Neutron diffraction in situ monitoring of the dislocation density during martensitic transformation in a stainless steel. Scr Mater 2013;68:506–9. https://doi.org/10.1016/j.scriptamat.2012.11.031.
[16] Choi JY. Diffusion of hydrogen in iron. Metall Trans 1970;1:911–9. https://doi.org/10.1007/BF02811773.
[17] Fuchigami H, Minami H, Nagumo M. Effect of grain size on the susceptibility of martensitic steel to hydrogen-related failure. Philos Mag Lett 2006;86:21–9. https://doi.org/10.1080/09500830500482316.
[18] Liu Y, Wang M, Liu G. Hydrogen trapping in high strength martensitic steel after austenitized at different temperatures. Int J Hydrogen Energy 2013;38:14364–8. https://doi.org/10.1016/j.ijhydene.2013.08.121.
[19] Barrera O, Bombac D, Chen Y, Daff TD, Galindo-Nava E, Gong P, et al. Understanding and mitigating hydrogen embrittlement of steels: a review of experimental, modelling and design progress from atomistic to continuum. J Mater Sci 2018;53:6251–90. https://doi.org/10.1007/s10853-017-1978-5.
[20] H.K.D.H. Bhadeshia. Prevention of Hydrogen Embrittlement in Steels. ISIJ Int 2016;56:24–36.
[21] San Marchi C, Somerday BP, Tang X, Schiroky GH. Effects of alloy composition and strain hardening on tensile fracture of hydrogen-precharged type 316 stainless steels. Int J Hydrogen Energy 2008;33:889–904. https://doi.org/10.1016/j.ijhydene.2007.10.046.
[22] Momotani Y, Shibata A, Terada D, Tsuji N. Hydrogen Embrittlement Behavior at Different Strain Rates in Low-carbon Martensitic Steel. Mater Today Proc 2015;2:S735–8.

https://doi.org/10.1016/j.matpr.2015.07.387.
[23] Agyenim-Boateng E, Huang S, Sheng J, Yuan G, Wang Z, Zhou J, et al. Influence of laser peening on the hydrogen embrittlement resistance of 316L stainless steel. Surf Coatings Technol 2017;328:44–53. https://doi.org/10.1016/j.surfcoat.2017.08.037.
[24] Wang Y, Wu X, Zhou Z, Li X. Numerical analysis of hydrogen transport into a steel after shot peening. Results Phys 2018;11:5–16. https://doi.org/10.1016/j.rinp.2018.08.030.
[25] Wang Y, Xie H, Zhou Z, Li X, Wu W, Gong J. Effect of shot peening coverage on hydrogen embrittlement of a ferrite-pearlite steel. Int J Hydrogen Energy 2020;45:7169–84. https://doi.org/10.1016/j.ijhydene.2020.01.021.
[26] Huang S, Ma D, Sheng J, Agyenim-Boateng E, Zhao J, Zhou J. Effects of laser peening on tensile properties and martensitic transformation of AISI 316L stainless steel in a hydrogen-rich environment. Mater Sci Eng A 2020;788:139543. https://doi.org/10.1016/j.msea.2020.139543.
[27] Takakuwa O, Soyama H. Suppression of hydrogen-assisted fatigue crack growth in austenitic stainless steel by cavitation peening. Int J Hydrogen Energy 2012;37:5268–76. https://doi.org/10.1016/j.ijhydene.2011.12.035.
[28] Takakuwa O, Nishikawa M, Soyama H. Numerical simulation of the effects of residual stress on the concentration of hydrogen around a crack tip. Surf Coatings Technol 2012;206:2892–8. https://doi.org/10.1016/j.surfcoat.2011.12.018.
[29] Chomienne V, Valiorgue F, Rech J, Verdu C. Influence of ball burnishing on residual stress profile of a 15-5PH stainless steel. CIRP J Manuf Sci Technol 2016;13:90–6. https://doi.org/10.1016/j.cirpj.2015.12.003.
[30] Loh NH, Tam SC. Effects of ball burnishing parameters on surface finish-A literature survey and discussion. Precis Eng 1988;10:215–20. https://doi.org/10.1016/0141-6359(88)90056-6.
[31] Avilés R, Albizuri J, Rodríguez A, López De Lacalle LN. Influence of low-plasticity ball burnishing on the high-cycle fatigue strength of medium carbon AISI 1045 steel. Int J Fatigue 2013;55:230–44. https://doi.org/10.1016/j.ijfatigue.2013.06.024.
[32] Mahmood Hassan A, Al-Dhifi SZS. Improvement in the wear resistance of brass components by the ball burnishing process. J Mater Process Technol 1999;96:73–80. https://doi.org/10.1016/S0924-0136(99)00254-X.
[33] Saldaña-Robles A, Plascencia-Mora H, Aguilera-Gómez E, Saldaña-Robles A, Marquez-Herrera A, Diosdado-De la Peña JA. Influence of ball-burnishing on roughness, hardness and corrosion resistance of AISI 1045 steel. Surf Coatings Technol 2018;339:191–8. https://doi.org/10.1016/j.surfcoat.2018.02.013.
[34] Kermouche G, Rech J, Hamdi H, Bergheau JM. On the residual stress field induced by a scratching round abrasive grain. Wear 2010;269:86–92. https://doi.org/10.1016/j.wear.2010.03.012.
[35] Alnajjar M, Christien F, Bosch C, Wolski K, Fortes AD, Telling M. In-situ neutron diffraction study of wrought and selective laser melted maraging stainless steels. Mater Charact 2021;172:110840. https://doi.org/10.1016/j.matchar.2020.110840.
[36] Tiphène G, Baral P, Comby-Dassonneville S, Guillonneau G, Kermouche G, Bergheau J-M, et al. High-Temperature Scanning Indentation: A new method to investigate in situ metallurgical evolution along temperature ramps. J Mater Res 2021;36:2383–96. https://doi.org/https://doi.org/10.1557/s43578-021-00107-7.
[37] Pérez Escobar D, Duprez L, Atrens A, Verbeken K. Influence of experimental parameters on thermal desorption spectroscopy measurements during evaluation of hydrogen trapping. J Nucl Mater 2014;450:32–41. https://doi.org/10.1016/j.jnucmat.2013.07.006.
[38] Fressengeas C, Beausir B, Kerisit C, Helbert AL, Baudin T, Brisset F, et al. On the evaluation of dislocation densities in pure tantalum from EBSD orientation data. Mater Tech 2018;106. https://doi.org/10.1051/mattech/2018058.
[39] Suresh S, Giannakopoulos AE. A new method for estimating residual stresses by instrumented sharp indentation. Acta Mater 1998;46:5755–67. https://doi.org/10.1016/S1359-6454(98)00226-2.

[40] Frutos E, Multigner M, González-Carrasco JL. Novel approaches to determining residual stresses by ultramicroindentation techniques: Application to sandblasted austenitic stainless steel. Acta Mater 2010;58:4191–8. https://doi.org/10.1016/j.actamat.2010.04.010.
[41] Breumier S, Villani A, Maurice C, Lévesque M, Kermouche G. Effect of crystal orientation on indentation-induced residual stress field: Simulation and experimental validation. Mater Des 2019;169:107659. https://doi.org/10.1016/j.matdes.2019.107659.
[42] Tabor D. The hardness of metals. Oxford uni. 2000.
[43] Wei FG, Tsuzaki K. Response of hydrogen trapping capability to microstructural change in tempered Fe-0.2C martensite. Scr Mater 2005;52:467–72. https://doi.org/10.1016/j.scriptamat.2004.11.008.
[44] Turk A, Joshi GR, Gintalas M, Callisti M, Rivera-Díaz-del-Castillo PEJ, Galindo-Nava EI. Quantification of hydrogen trapping in multiphase steels: Part I – Point traps in martensite. Acta Mater 2020;194:118–33. https://doi.org/10.1016/j.actamat.2020.05.007.
[45] Sofronis P, McMeeking RM. Numerical analysis of hydrogen transport near a blunting crack tip. J Mech Phys Solids 1989;37:317–50. https://doi.org/10.1016/0022-5096(89)90002-1.
[46] Krom AHM, Koers RW., Bakker A. Hydrogen transport nea a blunting crack tip. J Mech Phys Solids 1999;47:860–81.
[47] Makoto K, Wataru U, Satoshi Y. Improved hydrogen embrittlement resistance of steel by shot peening and subsequent low-temperature annealing. ISIJ Int 2021;61:1159–69. https://doi.org/10.2355/isijinternational.ISIJINT-2020-463.